Impact of Laser-Induced Oxidation on Laser-Induced Damage Thresholds of Copper Thin Films

Hsiu-Min Wu 12321966

16-08-2024

Abstract

Laser-induced damage studies have applications in optical techniques using high-powered lasers, such as materials processing and metrology. Here we investigate laser-induced chemical changes using thin copper films exposed to a nanosecond UV laser due to their prevalence in electronics and material processing. In particular potential oxidation with atmospheric oxygen is studied due to Cu's readiness to form oxide species (Cu_2O, CuO and $Cu(OH)_2$). Regions exposed to different laser fluences in ultra-high vacuum, 10^{-2} mbar O_2 and air are characterized using optical microscopy to determine their damage threshold. The surface composition and oxidation state changes of the Cu layers close to the damage threshold are analyzed using ex situ X-ray Photo-electron Spectroscopy (XPS). The results show significant differences in damage behavior for UV illumination in ambient versus ultra-High vacuum, confirming the significance of atmospheric effects. XPS results suggest a possible systematic reduction of divalent Cu oxide species due to UV exposure, which can be the result of multiple damage-related mechanisms such as water film evaporation and different ablation thresholds of different species.

Contents

1 Background

Pulsed lasers have been utilized in a variety of fields for their unique properties. Short pulses provide small timescales,in the nanosecond range or lower, that can be used to monitor ultra-fast processes like lifetimes of electronic excited states via fluorescence decay pump probe measurements [1]. In addition, their typically high intensities allow for the utilization of nonlinear optical effects e.g. second harmonic generation for detecting non-centrosymmetric crystals [2]. Unfortunately, such high intensities often cause laser-induced damage (LID) that limits the kinds of samples that can be measured in such a manner and limit said sample's exposure time [3]. This is especially significant for samples with microscopic structures such as thin films and etched silicon wafers; such materials have a lower effective LID due to different laser-matter interactions. One of the most common mechanisms for LID is thermal ablation, where the laser energy is converted to heat, effectively increasing the material temperature above its melting point so rapidly, that the melted material is forcefully removed. Depending on the properties of the laser pulse and the material, other damage mechanisms can be prevalent, like laser-induced breakdown in dielectrics for picosecond (or smaller) laser pulses; thermal damage occurs for all laser pulses [4]. The exact fluence threshold(s) for such damage varies depending on the pulse duration and material properties.

1.1 Laser Thermal Damage

The basic principle of laser thermal damage is fairly straightforward: The material heats up by the illumination. Once a specific temperature T is reached, the material changes phase. Any light-source, coherent or not, can do this. The extent to which is happens is governed by the refractive index $n + ik$ of a given material, which varies depending on the wavelength received. Here the real part determines the amount of reflection when the light hits the surface of the material of interest (here on referred to as the sample) given a incidence angle θ. This reflection depends on the refractive indices of the medium light was traveling in and the illuminated material, the polar-

ization(s) of the light, and the angle of incidence. This is governed by the Fresnel Equations. Once the electromagnetic wave enters the sample, the imaginary part k determines the amount of attenuation, typically a exponential decay as described by the Beer-Lambert Law $I = I_0 e^{-4\pi kd/\lambda}$ as a function of the wavelength λ, absorption coefficient i.e. k, depth within the material d and the initial intensity I_0. To estimate the total energy however, one also needs to consider the pulse width, or lack thereof in the continuous wave case, of the laser. The precise estimation depends on the shape of the pulse and the pulse width. CW lasers are the simplest with simply the amount of time the surface is illuminated. The combination of all of this tells you the total energy absorbed by the sample, to which one can convert into heat using material properties under a heat equation.

Two constants are of importance in determining the temperature of a material: the heat capacity C and thermal conductivity κ. Heat capacity sets the amount of energy needed to change a material's, of a specific quantity, temperature(can be either in terms of volume $C_v = \frac{C}{V}$ or mass $C_M = \frac{C}{M}$). Thermal conductivity determines the rate at which the heat is conducted through the material. The latter is important as the laser only heats up a region of the sample, from which heat is distributed. A high κ results in fast conduction and thus a more even increase of T given a specific C. A useful measure is to combine these two with the density ρ of your material into the thermal diffusivity $\alpha = \frac{\kappa}{\rho C_M}$, which gives a general rate of heat transfer of the sample. This can then be used along with the laser energy, time and material size to produce a heat map of the sample using the heat equation that best describes the system. From here a basis is formed for simple change of phase i.e. melting and vaporization, and more exotic thermal-derived effects.

Usage of pulsed lasers can lead to more exotic thermal effects than the CW case due to the high power. It is much easier to deposit a large amount of energy in very short time with the former, which can create complications in the temperature map. This is due to the fact that the density of any given material changes with heat, especially when change of phase occurs. This thermal expansion is typically described for each material by the thermal expansion coefficient $\alpha = \frac{1}{V}(\frac{dV}{dT})_P$. For materials with a high

α, Local expansion of the material can deform it readily, such as asphalt during a hot summer. Should the local heating be sufficiently intense, the rapid expansion and cooling can lead to portions of the sample ejected from the surface. This phenomenon has long be taken advantage of as a method of material deposition e.g. excimer-based pulsed laser deposition [5].

1.2 Laser-Induced Oxidation

Thermal damage thresholds and the associated damage mechanisms have been investigated for a variety of materials under certain environmental factors. Materials under different ambient media, such as metals like gold and dielectrics like quartz under air and water, have been tested [6, 7]. Investigations have also been done on materials in both bulk and film form for comparison. The latter, along with other forms of microscopic structures, are often more susceptible to heat damage [8]. The effects of ambient medium adsorption onto samples have also been studied. In particular water vapor in porous samples that were in contact with air have been demonstrated to be a strong reducing force in LID thresholds under vacuum conditions [9]. What is unknown is if potential chemical changes as a result of the sample interacting with the atmosphere due to laser heating has an impact on said threshold(s).

The principle behind Laser-Induced Oxidation (LIO) is also quite simple: chemical reaction rates tend to be faster when provided thermal energy. This is largely due to higher collision rates between molecules and overcoming the activation energy should it applies. If the surface has adsorbed reagents on its surface or regular collisions from the surrounding medium e.g. air, chemical reactions can be induced or encouraged by the additional heat provided. In addition given a sufficiently high energy the adsorbing compound(s) may disassociate into elements that can react with the sample. The latter is highly dependent on the concentration, absorption coefficient and cross section of the adsorbent in question. Chemical reactions induced in the former manner can typically be characterized with the Arrhenius Equation:

$k \approx k_0 e^{-E_a/k_B T}$, where the rate constant of a reaction k is determined by the base rate constant of said reaction k_0, the activation energy E_a and the temperature. Though temperature changes the rate exponentially, the precise rate of increase of the reaction rate depends on the rate equation of the specific reaction.

1.3 Material and Radiation of choice

To study the aforementioned LIO, one must pick a material, a laser and the environment the sample can react with. Here we chose to use an excimer laser (248nm) for illuminating Copper to investigate Laser-Induced Oxide Formation. The reasons for this specification are provided below.

1.3.1 UV Excimer (Exciplex) Laser

An Exciplex laser is a high-intensity pulsed laser produced using a gaseous unstable lasing medium. It is typically a mixture of a halogen gas (Fluorine or Chlorine) and a noble gas. This mixture is electronically stimulated to form a unstable compound between the halogen and noble gas, also called an exciplex. These unstable compounds emit a specific wavelength when they disassociate via spontaneous/stimulated emission, and return to their original states. By forming a population of exciplexs proportionally larger than the remaining original mixture, stimulated emission as pulses can be achieved in a consistent cycle. To encourage exciplex formation a third buffer gas (Xe or H) is often added. As the disassociation happens in the span of nanoseconds, this allows the formation of a nanosecond pulse of high intensity typically in the UV range, which is very useful for its wavelength.

A UV laser is useful for depositing a high amount of energy in a small region for most materials. This is because the typical penetration depth $d_p \rightarrow \frac{1}{e} I_0 = I_0 e^{4\pi k d_p/\lambda}$ for UV lasers are quite small due to the short wavelength and most material's high absorbance of the material [10]. This makes it useful for purposes requiring fine features e.g. micromachining and eye surgery [10]. For our investigation it means that a significant portion of the energy will be absorbed near the surface, encouraging Laser-induced oxidation with the sample and allows for efficient thin-film illumina-

tion (It should be noted that its absorptive property is also a curse, as focusing and delivering the beam without losing much of it to the optical components is tricky). In addition due to the absorptive properties little of the beam is lost due to reflectance.

1.3.2 Copper

Copper is a very useful material to study LIO due to its readiness to oxidize, its broad applications and availability. Like many other metals e.g. Iron and Lead, Copper oxidizes continuously at room temperature in air, and is known to oxidize faster when heated. For testing oxide formation e.g. CuO, one of the most common oxidations on the planet due to air, it is easy to induce it; simply heating a chunk with a Bunsen burner would do. It is also a material with broad electronic applications; a regular guest under material processing and metrology. It has been reported that copper forms different kinds of oxides depending on temperature; Cu2O for room-temperature oxide formation and CuO for at temperatures >500K. In addition it has been reported that Cu(OH)2 forms as a result of water films adsorbed on a copper surface. For the latter a further understanding of the impact of chemical interactions on laser damage can be useful for pulsed-laser based metrology.

1.4 Surface Characterization Methods

To quantify laser damage and oxidation of sample, we employ Bright-Field (BF) and Dark-Field (DF) microscopy for the former and X-Ray Photo-electron Spectroscopy for the latter. This is necessary as a quantitative difference in damage must be established to show the potential impacts of oxidation, and to show oxidation i.e. oxide growth surface characterization of the sample is needed. For the two optical techniques the Zeiss Online Campus is used heavily as reference [11]. For X-ray Photo-electron Spectroscopy Introduction to x-ray photoelectron spectroscopy by Stevie et al. and *Surface Science: An Introduction* by K. Oura et al. are used exten-

sively as reference [12, 13].

1.4.1 Optical Microscopy

Of the many imaging techniques that have been developed and used for Surface characterization, Bright Field and Dark Field has been around the longest. BF is but another name for the default optical microscopy, its basic form existing for as long as optical microscopy. DF meanwhile has been in scientific use for more than a century. These imaging techniques, while much coarser in resolution ($\approx 0.2\mu m$ as the diffraction limit) than other modern counterparts, are nevertheless still very useful for quick and intuitive characterization [11]. Each have their own advantages and disadvantages, thus a combination of both is desired for this investigation. Due to the nature of our sample here we only focus on reflected light microscopy (also known as epi-illumination) i.e. light reflecting from the sample back into the apparatus.

A Optical Microscope (OM), in its essence, is a combination of two magnifying glasses and a light-source. Light is procured from a source, sometimes from ambient or a lamp, which is then focused onto the sample with a condenser. A simple description of its function is like using a magnifying glass to focus sunlight at a point. After light reaches the sample and is reflected back, an objective collects that light and magnifies the image. This image is then transmitted into a camera or an ocular. For epi-illumination the condenser and objective are combined into one. Here the reflected light leaves the objective as a parallel beam until it enters a tub lens, which then focuses the light and forms the image for observation. This simplistic setup makes it a versatile method, but is heavily limited by lens properties.

There are two major issues that befuddles OM in general: the diffraction limit and aberrations. The first is the limitation caused by the fact that light entering a small aperture will diffract. This is typically described classically under the Huygens principle, in which light of a particular wavefront can be considered to be composed of individual wavelets, which form spherical waves when the path is disturbed e.g. a change in n or a slit. These waves collectively form the new wavefront due to

interference. In the most simplest case i.e. a point source of light, an airy disk is formed where the center peak is the zeroth order reflection and the surrounding waves addition diffraction orders. To distinguish between two sources e.g. two different spots in a image, the limiting factors are the width of the airy disks' peaks and the distance between the disks. The former is determined by the wavelength, as the smaller it is the the angle between the diffracting order and zeroth order is smaller, resulting in a thinner peak due to destructive interference. The latter is determined by the Numerical Aperture (NA) of the objective and condenser (for epi-illumination the same), as the larger it is the wider the field of view of the two lenses are leading to more precise angular resolution. A description of this can be found under the Abbe diffraction limit $d = \frac{\lambda}{1.22NA}$, in which d is the minimum distance between the two point sources. Conventional Microscopes typically allow up to $NA = nsin[\theta] = 1.4$ by using immersion oil to increase the refractive index and multiple lenses to increase the accepted angles $\theta_a = 2\theta$. The increase of this angle, however, can worsen the second effect without corrections.

If the diffraction limit restricts the differentiation of different structures, aberrations limit the representation of them. It describes a class of imperfections that is due to a lack of uniform foci for all collected light. There are many kinds of aberrations, but in general they can be separated into two groups: chromatic and monochromatic. The former are imperfections of the image that stems from the refractive index n. This is due to the fact that for glass the refractive index changes within the visible wavelength range, which in turn changes the angle at which the individual wavelengths propagate through and exit the lens (described by Fresnel Equations). This effect becomes more pronounced the larger the incident angle is compared to the plane of incidence, which is desired for a smaller diffraction limit. Whereas monochromatic aberrations are typically due to the curvature of the lens and the alignment of the lens relative to the sample. Chromatic aberrations are corrected using apochromatic lenses, which are designed to focus red, green and blue light to the sample foci. Achromatic lenses, ones that focus two instead of three wavelengths to the same foci, are also in use though provide less corrections. For monochromatic

aberrations a mixture of techniques are used depending on the precise aberration, ranging from quality control for perpendicular optical axes and sample stage (relative to the incidence plane) to having multiple lenses. Since these issues stem from optical properties of the lenses and other parts of the setup, it is also applicable to Dark Field Microscopy.

Dark Field Microscopy differs from the default OM in two ways: indirect illumination of sample (also called oblique illumination) and removal of the zeroth order when the image enters the ocular/camera. The principle is to limit the amount of total light reflected by illuminating the sample at an angle e.g. a ring of light that focuses at the sample, and then only transmit light that is scattered i.e. light leaving the sample with an angle not equal to the incidence angle. For epi-illumination this is done by using a circular beam block and a collection of ring-shaped mirrors to focus a ring of light onto the sample with a incidence angle larger than the field of view of the objective. Thus the latter only collects light that is the result of scattering, as the actual reflected beam does not enter it. This is particularly useful for characterizing local morphologies of a nominally flat surface, something that BF cannot do adequately.

Dark-Field and Bright Field (OM) Microscopes each have their own role for surface characterization. For BF as only the reflected light returns to the OM, the features it can characterize are changes in reflectivity, visualized as a difference in color. This is useful for identifying different substances or structures with different refractive indices. For changes that maintain the same reflectivity, however, it can only identify those that reflects less light back either due to the geometry or simply destructive interference with the surrounding light; the zeroth order beam drowns out the smaller signals. This is not an issue for DF, where the main beam is discarded after sample illumination and only scattered light remain. Thus structures that scatter light the strongest will have the largest signals based on their shape instead of the wavelengths it reflects. This is at the cost of knowing the reflectivity map of the sample. Luckily modern epi-illumination techniques are able to merge these under one microscope. These can switch to different modes with a flick of the finger with modular mirror assemblies and complicated objectives that automatically changes modes based on

the illumination it receives from the mirror assembly of choice. This makes it very useful for characterizing our Copper surface for removal of said element, as uniform removal will result in a strong signal in BF and small, local removal results in a strong signal in DF. These techniques can then be used to characterize morphological changes as a function of fluence, which can then be corresponded with chemical changes using the X-Ray Photo-electron Spectroscopy.

1.4.2 X-ray Photo-Electron Spectroscopy

X-ray Photo-electron Spectroscopy (XPS) is a technique widely used for detecting chemical composition of a given sample. Since the first proof of feasibility with the measurement of NaCl spectra by K. Siegbahn in 1954, XPS has been a widely used technique for both in-situ and ex-situ characterization of chemical reactions [14]. It is based off of the photoelectric effect as described by Einstein five decades before its invention.

The photoelectric effect describes the process of electron emission from a given material due to optical illumination. Electrons are bound to a given solid material by two different energies: The work needed to remove/add an electron to the solid i.e. work function (ϕ), and the work needed to remove an electron from the orbital it resides in i.e. Binding Energy (E_B). If sufficient energy is put into the system as a result of photon illumination (with some energy $E_p = hf$, h being the Planck constant), electrons can then be ejected with some kinetic energy $E_K = hf - (E_B + \phi)$. Note that since $E_K > 0$ there is a lower limit for hf that is dependent on material properties. The With a monochromatic source and an electron analyzer one can then measure the distribution of electrons in terms of E_K, which with prior knowledge of each element's binding energy and the work function can be translated into a measure of elemental composition.

Photoelectron Spectroscopy takes advantage of the uniqueness of each element's electronic properties to find information on chemical binding energies. As the distribution of electrons across orbitals is unique for every element, the binding energies for each element are unique even for within same orbital between elements. Fur-

thermore should there be chemical bonding between elements E_B should change depending on the bonding type and bonded elements. Given a uniform illumination, detected electronic signals should correlate to concentrations of each element in the sample. This allows for chemical characterization of compounds and mixtures that have an unknown formulae. For XPS, the electrons of interest is on core electrons and auger emission.

XPS focuses on core electron and auger emission, as a consequence of the former, detection which allows for better clarity in chemical analysis. Binding Energies easily shifts for valence electrons depending on the type of chemical bond and the element(s) bonded together, which can be difficult to entangle when the rough chemical composition is not known. In addition depending on the bonding the valence electrons can roam around e.g. metallic bonding, reducing the correlation between detected electrons' signal and chemical composition. Core electrons do not suffer from these problems as their shifts are much smaller and are relatively fixed. Thus one can detect both the presence of specific elements and the oxidation states i.e. the ionic states at the same time. Note that the removal of core electrons tend to be accompanied by Auger emission, where a valence electron is further emitted from the system as a result of compensating for the core electron loss. These emissions also result in peaks that are correlated to material composition. This combination of these peaks can further the precision of XPS-based chemical analyses. To rip out the electrons X-rays of multiple keVs are used as they are sensitive to core electrons more than valence ones, resulting in a high surface sensitivity.

XPS has high surface sensitivity primarily due to low electron attenuation depths. This is primarily due to scattering within the sample. X-rays can penetrate up to micrometers into a sample, producing photoelectrons on the sample's surface and inside it. Photoelectrons produced inside the sample have a chance to collide with other atoms before leaving the sample, resulting in a long tail following every peak in XPS spectra due to energy loss. This produces a step-like background for all XPS survey spectra, where one measures a largest range of E_B the source allows for. The chance of collision is characterized by the attenuation length λ_a, the mean free

path for an electron of a specific energy to escape the sample without losing energy. Precise definitions of this system depends on the amount of inelastic and elastic scattering of the system, which is a field of its own. Nevertheless this can usually be approximated with the inelastic mean free path λ_i, assuming all collisions are inelastic. This along with a formulation of the Beer-Lambert Law $I = I_0 e^{d/\lambda_i}$ allows one to estimate at what depth does the electron contribution becomes negligible with some pre-defined threshold. Calculations have shown that 95% of the electronic signal comes from the first 10nm or less for any given material [12]. This makes XPS very useful for chemical analyses for sample surfaces.

High surface sensitivity accompanied by relative clarity of different oxidation species makes XPS invaluable for copper oxidation. Should Laser-Induced Oxidation be detectable, the level of oxidation should correspond with the energy distribution under illumination. As we expect a low penetration depth with the 248nm pulse, any oxide formation or other oxidation should be easily detectable at the Cu surface. By picking a substrate copper is unlikely to react with, such as silicon, one can then limit the kinds of oxidation to that of between ambient oxygen and water films. This can be done by capturing the Cu2p and O1s spectra, which provides the highest signal for the respective elements. This allows for a simple measurement of Oxide growth by calculating the change in total intensity ratio between Cu2p and O1s. This can be done by fitting the respective spectral data and integrate over the fitted peaks. In addition oxidation species can be identified with a mixture of aforementioned spectra and Cu auger (CuL3M45M45) spectra as have been done in literature [15].

2 Introduction

High-powered pulsed lasers find application in a variety of optical techniques, from measurement techniques, such as interferometric metrology and laser-induced ultrasound scanning, to ablative techniques like pulsed laser deposition and micromachining[5, 16–19]. These techniques are often limited by unintentional modifications of samples and optical components as a result of laser exposure, resulting in inaccurate measurements[17]. Therefore it is important to determine the threshold at at which material properties change in terms of laser fluence. Multiple kinds of damage can occur on a material e.g. ablation and dielectric breakdown, each having its own distinct fluence threshold[4]. Each of these thresholds are laser and material dependent. These include but are not limited to the laser profile, sample properties e.g. shape, size and composition, and the environment it is illuminated in. The latter is relevant as the energy provided by illumination can induce chemical reactions between the illuminated area and chemical elements surrounding them e.g. Oxygen in the atmosphere[20].

Laser-induced damage studies have been done frequently on copper as it is widely used in electronics and thus regularly studied in the context of micro-machining and high-powered laser-metrology [21, 22]. Due to the prevalence of Ultraviolet (UV) lasers in deposition and material processing multiple studies have been done on vacuum bulk copper ablation thresholds at certain wavelengths under UV [5, 23–25]. In addition studies of ablation under air has been done to observe the effects of laser-induced oxidation [26]. These are typically done on bulk copper or copper-dominant alloys under the context of material processing. A common trend is the identification of Laser-Induced Oxidation (LIO) of bulk copper from oxygen and water films, and the interplay between LIO and laser-induced plasma plumes where proposed [26, 27]. Copper oxides formed from these effects have a lower ablation threshold when compared with Cu(0) due to a lower thermal conductivity and thus can be selectively removed [28].

In contrast to bulk copper, effects of laser-induced oxidation on copper thin films are currently unknown. While laser-induced damage studies have been done on copper films, these typically have micrometer thickness and down to hundreds of nanometers [25]. For more delicate structures, ones in the tens of nanometers seen in electronic components e.g. semiconductor chips, the ablation threshold and impact of LIO under Ultraviolet wavelengths are not well known both qualitatively and quantitatively.

Here, we exposed sub-50 nm Cu thin films are exposed to a pulsed UV laser with systematically varying fluence per pulse, number of pulses, and Oxygen pressure. The fluence threshold for laser induced damage is determined for each condition using optical microscopy and is found to decrease from vacuum to atmosphere. Moreover, the connection between laser-induced damage and surface chemical changes measured by photoelectron spectroscopy is investigated.

3 Methodology

3.1 Sample Preparation

Polycrystalline copper thin films of 30 [nm] were deposited via the Electron-beam physical vapor deposition method (Polyteknik Flextura M508 E) onto Silicon substrates cleaned with base Piranha (12 [mm] by 12 [mm]). Said substrates have a native oxide layer due to ambient exposure. During deposition a mask is placed in front of each substrate. This results in the formation of three by three grid as shown below:

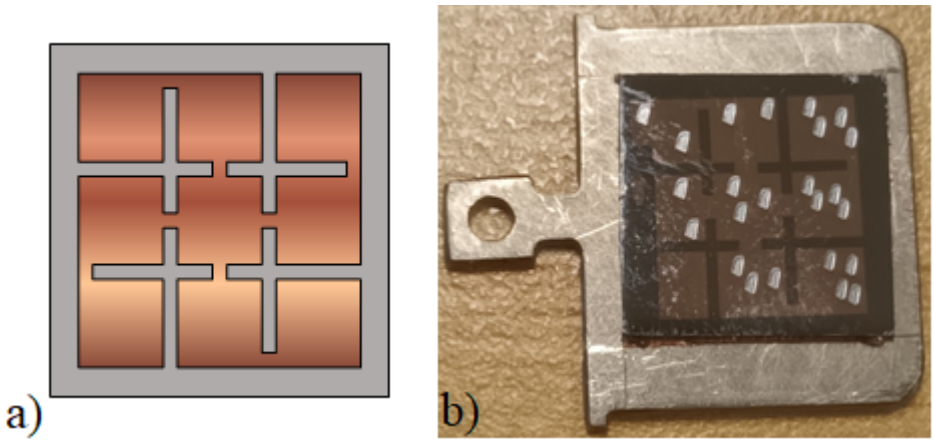

Figure 1: Graphical depiction of a 10 [mm] by 10 [mm] copper film on top of a 12 [mm] by 12 [mm] Silicon substrate (a) & real life example of such a film (b). Note that in the lower left the film has a cutoff; this is due to the design of the substrate holder for the E-beam deposition process.

This particular geometry creates nine square target areas for the UV laser. The squares are connected to keep them grounded when making X-ray Photo-electron Spectroscopy (XPS) measurements. Samples are mounted onto a Stainless steel plate with conductive copper tape as shown in the figure for experimentation.

3.2 Experimentation Setup

Illumination of copper samples will be done using a setup for pulsed laser deposition:

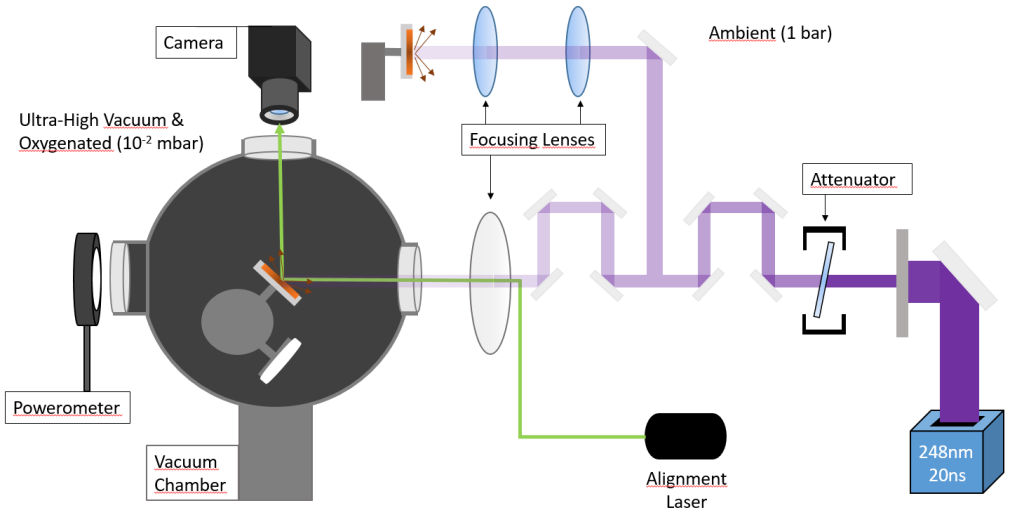

Figure 2: A simplified description of the experimental setup. A UV pulsed laser beam illuminates a mask, followed by an attenuator and is imaged onto one of two target positions, in ambient and in a UHV chamber.

For experiments below atmospheric pressure, Cu samples were loaded onto a sample stage in a vacuum chamber with a base pressure below 10^{-9} [mbar]. The stage has 4 degrees of freedom (x,y,z, 360 [deg] rotation) for movement with sub-millimeter precision. A high-precision leak valve allows setting well-defined gas pressures and is used for experiments in oxygen pressures below ambient. A series of 10 mirrors and a focusing lens is used to guide and focus the UV pulse into the chamber and image the shape of a rectangular mask onto the sample. Ambient experiments were performed with an additional lens and the sample placed in the laser beam path.

Ambient experiments are done with a setup installed on the beam path of the aforementioned vacuum setup. The sample stage has three degrees of freedom (x,y,z) and has micrometers precision. Two lenses with a much smaller focal length are used to focus the laser onto the sample. It should be noted that this alignment is independent of the vacuum chamber focusing lens. The focusing is done such that the same rectangular shape is imaged onto the sample as in vacuum.

3.3 Laser Profile

A COMPex 201 excimer laser is used to illuminate the Cu samples. The UV laser pulse has a wavelength of 248 [nm], ≈ 20 [ns] pulse length and has a max output of approx. 35 [mJ] at the vacuum chamber powermeter. The pulse has a roughly flat-top profile as it exits the source. This is further refined with the mask to select the region with higher intensities. To systematically vary the laser fluence an attenuator is used to reduce intensity via a polarizer. This allows testing for a fluence range from > 5 $[\mathrm{J/cm^2}]$ to < 0.1 $[\mathrm{J/cm^2}]$. A powermeter is used to measure before and after a round of experiment is done to determine the range where the deposited energy resides in. The powermeter has a lower detection limit of ≈ 2.5 [mJ].

3.4 Illumination Procedures for threshold characterization

Cu samples were exposed to UV light after they are loaded into the stage and the laser energy is checked with the powermeter. This is done under three different pressure regimes: 10^{-9} [mbar] (UHV), 10^{-2} [mbar] (oxygenated) and ambient. In addition three repetition modes were tested: single-shot, 10-shots and 100-shots per illuminated spot. To isolate the pressure variable single-shot mode was used for samples under UHV and ambient. To consider the effects of multi-shot modes on oxidation, samples were illuminated under ambient with 10- and 100-shots modes in addition to the single-shot spots. To aim the invisible UV laser at the desired spot in the vacuum chamber a continuous wave laser of 532 [nm] is aligned with it. Using a camera one can see the approximate spot of UV illumination is. For the ambient cases a trial and Error method is used to determine where the pulse would hit relative to the unit markings on the sample stage.

Shots are made on each pocket of the sample for vacuum experimentation. One of the pocket pockets is not illuminated, here on referred to as the pristine one, as a control for comparison. With an illumination area of $A_I = 0.04$ $[\mathrm{mm^2}]$ four shots can be easily fit within each pocket, resulting in 24 illuminated spots per sample on average. For ambient cases a grid-less copper film on Si substrate is used to the

same effect, with rows of illuminated spots for the single-, 10- & 100-shots regime respectively. The multi-shots regime have a repetition rate of 4 [Hz].

3.5 Identification & Characterization of laser damage

After illumination the Cu samples are removed from the steel plates and observed under an optical microscope (Zeiss Axioskop2 mat, epi-illumination). Using the camera (Microscope camera Axiocam MRC 5) installed on the microscope, the laser-exposed spots are imaged using Dark Field (DF) & Bright Field (BF) microscopy. These images are then used for visual inspection of structures and characterization of ablated area change as a function of fluence. For the latter DF images are primarily used due to the surface sensitivity; it can pick up local surface changes e.g. partial Cu removal whereas BF is more useful for identifying reflectivity changes and ablation.

3.6 Illumination Procedures for Material Composition Analysis

Illumination procedures for identifying chemical change have some variations to accommodate XPS limitations.To measure potential oxidation, samples are illuminated at the identified damage threshold as higher fluences can lead to material removal. As such all samples are illuminated at fluences % lower than the estimated damage threshold to account for fluence variations. In addition the X-ray Photo-electron Spectroscopy (XPS) have a approximate analysis area of 0.8 [mm] in diameter, much larger than $A_I = 0.04$ [mm^2] as used before. To have a higher signal to noise ratio the illuminated area is enlarged using alternative masks.

A elliptical mask was used for non-ambient samples which results in A_I with a width of 0.8 [mm] and height of 2 [mm]. Here each pocket contains one shot in the middle for ease of detection. The grid assists aiming in combination with a electron detector by detecting the copper, and lack there of on the grid, signal. This allows for identification of pocket boundaries, which one can then estimate the center where the illuminated spot is located. For oxygenated samples the aforementioned gas valve is used to leak O_2 gas into the chamber; a detector in the vacuum chamber is used to

keep track of the pressure. After illumination rounds are done the samples are moved directly from the vacuum chamber into the XPS with a internal vacuum-maintained transport mechanism. For ambient experiments the same type of copper film is used but with a different mask and spot locations.

A different rectangular mask is used to have a A_I of 0.5 [mm] in width and 1.5 [mm] in height. the center of each pocket is then illuminated with two spots as close to each other as possible using sample stage markings and the naked eye. With this a total illumination area with 1mm width is obtained, larger than the XPS detection range. BF Images are taken after illumination to check if there is any overlap.

3.7 Material Composition Analysis

X-ray Photo-electron Spectroscopy (XPS) is to identify sample chemical changes as a result of UV illumination. Here an Al Kα source (1486.6 [eV]) is used. A Scienta Omicron HiPP3 analyzer with a 1 [mm] entrance slit setting is used for spectral analysis. The approximate area of analysis is 0.8 [mm] in diameter, and measurements are done in vacuum with typical pressures of 10^{-8} [mbar].

In each XPS experiment, the following spectra are acquired: A survey spectrum (Pass Energy = 300 [eV]), detailed spectra of the Si2p (Pass Energy = 300 [eV]) and C 1s (Pass Energy = 100 [eV]) regions, and high-resolution spectra of the Cu2p, $CuL_3M_{45}M_{45}$ (auger spectrum) and O1s regions (Pass Energy = 100 [eV]).

4 Results

4.1 Visible changes of Illuminated copper Films

To determine the visible changes caused by laser illumination, an optical microscope with adjustable magnification was used to capture Dark-field (DF) and Bright-field (BF) images of UV-exposed copper films:

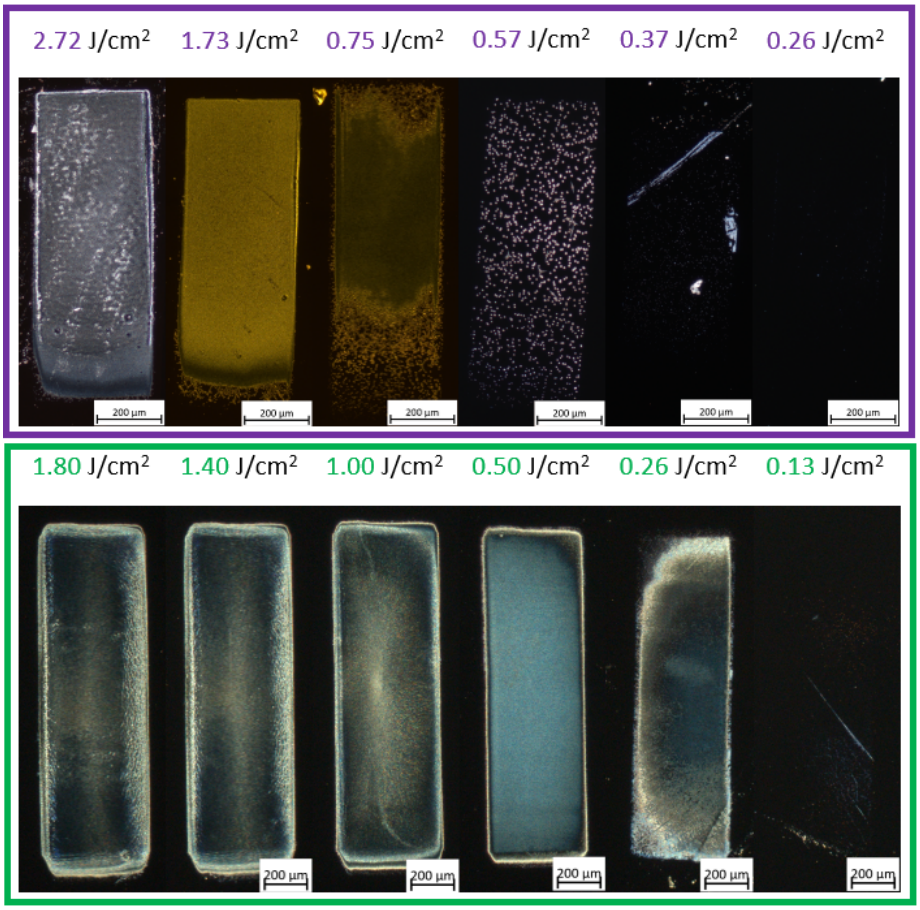

Figure 3: Optical Dark-field(10X magnification) images of copper surfaces illuminated by single-shot UV pulse in Ultra-High Vacuum (purple row) and in ambient (green row). Samples were illuminated in the fluence range from $4[\mathrm{J/cm^2}]$ to $< 0.01[\mathrm{J/cm^2}]$. Two of the images are taken under a UV filter, resulting in a yellow tint.

In Figure 3 surface changes of the illuminated areas within the ablation regime are shown for samples exposed under UHV and ambient conditions with varying fluences. Here a selection of images are chosen to represent the change in ablation behavior with varying fluences; some images are omitted for brevity. A general trend can be identified with higher fluences leading to a more uniform rectangular crater and lower fluences an assortment of spots within said rectangular area until no spots remain. Under UHV uniform ablation cease to dominate before $0.75[\mathrm{J/cm^2}]$ whereas for ambient samples this is still the case by $0.5[\mathrm{J/cm^2}]$. This difference in material removal is also the case for when spots i.e. local surface changes are no longer visible, with the vacuum case seen at $0.26[\mathrm{J/cm^2}]$ whilst ambient samples exhibit almost full uniform ablation at the same fluence. Note that the lines seen at $0.37[\mathrm{J/cm^2}]$ for vacuum and $0.13[\mathrm{J/cm^2}]$ for ambient are indicative of a scratched sample and not UV ablation behavior. In addition the laser alignment was far from perfect demonstrated by the visible gradient seen at $2.72[\mathrm{J/cm^2}]$ and $1.73[\mathrm{J/cm^2}]$ in vacuum and $0.5[\mathrm{J/cm^2}]$ in ambient. Bright-field images show the same evolution except at low fluences, where a rectangular discoloration is visible.

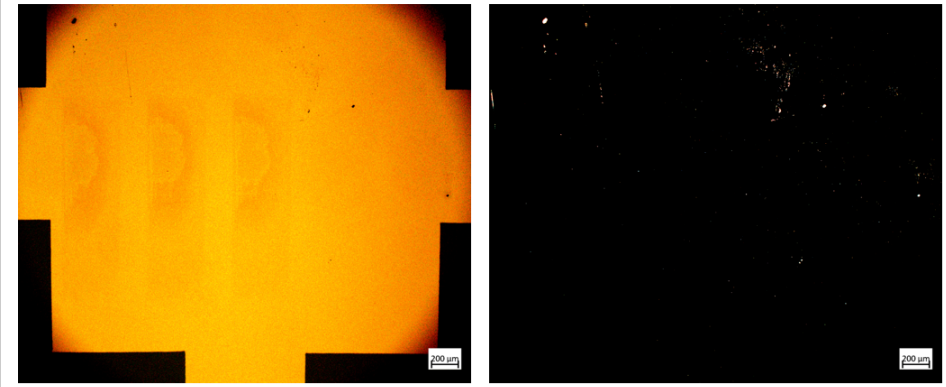

Figure 4: DF and BF Images of a single Cu pocket illuminated by single-shot UV pulse via optical microscope. All spots were illuminated under a fluence of $0.11[\mathrm{J/cm^2}]$. Note that both images here have a higher contrast compared to Figure 3. This was done using ImageJ to better visualize surface changes as seen under BF in contrast with lack of corresponding signal under DF.

Figure 4 hints at the different laser damage regimes at lower fluences. The BF image shows rectangular discolorations as suggested before, with a consistent gradient due to laser alignment. In contrast no significant signal is visible in the DF image despite increasing the contrast. As DF images are by design with higher contrast compared to BF, different sensitivities cannot be the explanation since both images are taken using the same microscope. Here a new damage regime is shown where removal of material is no longer detectable under Dark Field but the surface morphology exhibits changes in reflectivity under Bright Field. The transition between the two regimes shown in Fig. 3 and 4 is where we define the ablation threshold.

4.2 Quantification of Ablation Threshold

Using a combination of BF and DF images we quantify the proportional change of ablated area versus the detected fluence. Here ablation is determined as any bright spot under DF imaging that corresponds to damage seen under BF images. Thus the ablation threshold T_a is defined as when no DF signal is detected. This is important since as seen in Figure 4 the surface continues to be damaged i.e. changed when no DF signal is detected.

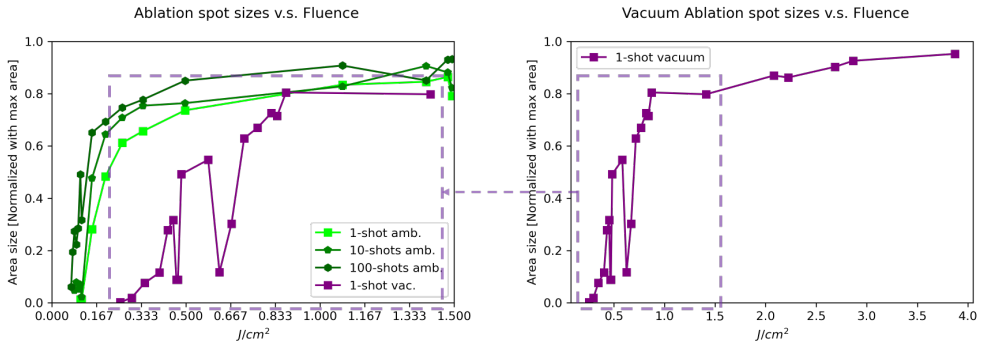

Figure 5: Relations between ablated areas and UV fluences (here on referred to as ablation curves) for samples illuminated under UHV and ambient. The UHV ablation curve (in purple) is shown both comparing to ambient regimes and by itself to demonstrate its broader trend. The ablated areas of respective regimes are normalized using the ablated area with the highest measured fluence for each regime.

In Figure 5 the ablated area as a function of fluence(hereon referred to as ablation curves) is compared for single-shot vacuum, single-shot ambient and multi-shot (10 shots and 100 shots, repetition rate of 4Hz) ambient regimes are shown. Here all ambient regimes have similar ablation curve slopes and T_a compared to the single-shot vacuum case. The 10-shots regime is visibly sandwiched between the single- and 100-shots regimes, an expected outcome as more shots equate more energy deposition thus a lower threshold. While all regimes have a logarithmic trend, the single-shot vacuum regime has a relatively flatter slope and higher threshold.
Quantitative calculations show a significant difference between ablation thresholds of single-shot vacuum and ambient regimes compared to single- and multi-shot regimes in ambient. Using a logarithmic fitting T_a were estimated for all regimes. Cu samples illuminated in vacuum show an ablation threshold of $T_a(p = 10^{-9}[\text{mbar}]) \approx 0.28[\text{J/cm}^2]$. Under ambient it is $T_a(p \approx 1[\text{bar}]) \approx 0.1[\text{J/cm}^2]$. This is quite different when compared to the ablation threshold difference between samples illuminated under single- and multi-shot regimes in ambient: the difference between single-shot and 100-shots ablation threshold is $\frac{0.1[[\text{J/cm}^2]]-0.08[[\text{J/cm}^2]]}{0.1[[\text{J/cm}^2]]} = 20\%$. This is more than three times smaller than the difference between ambient and vacuum single shot regimes; $\frac{0.28[[\text{J/cm}^2]]-0.1[[\text{J/cm}^2]]}{0.28[[\text{J/cm}^2]]} \approx 64\%$.

4.3 Material Composition

Using X-ray Photo-electron Spectroscopy (XPS) we identify potential material composition differences of illuminated copper film regions with fluences near the ablation threshold ($\approx 10\%$ lower due to fluence variations). This range shows visible surface changes yet no detectable removal of copper as seen in Fig. 4, increasing the chances of finding potential oxidation. Here in addition to UHV and ambient pressures an additional oxygenated regime, 10^{-2} mbar of O_2, is introduced to quantify potential trends of compositional differences versus O_2 pressures. To have a shared point of reference all the spectra are normalized with the Cu2p spectra. Cross section corrections are applied when necessary. For identifying peak positons the *Handbook of X-ray Photonelectron Spectroscopy* and Advanced analysis of copper X-ray photo-

electron spectra by Biesinger et al. are used extensively. [**moulder_handbook_1992**, 15] The former is used to identify elements from the survey spectra and the latter for copper oxidation species.

4.3.1 From Ultra-High Vacuum to Ambient

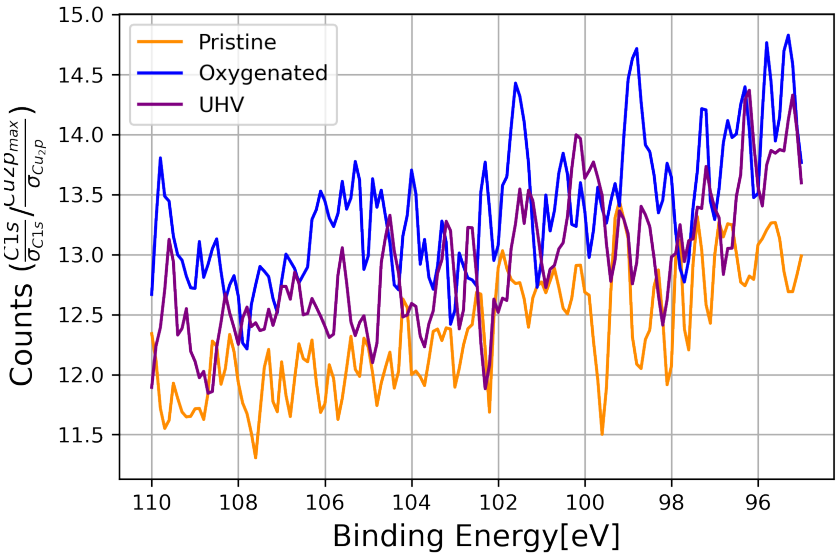

Figure 6: Si2p spectra (Pass Energy (PE) = 300 [eV]) from a sample with a pristine region and two regions illuminated in UHV and oxygenated conditions respectively. All intensities are normalized to the respective Cu2p maximum signal with cross section σ corrections

For Figure 6 a selection of Si2p spectra are depicted. They are normalized with respective to the Cu2p spectra from the same region with cross section σ corrections. No consistent peaks wider than noise were identified despite using a lower energy resolution setting (PE=300eV). In particular no Si(0) or SiO_2 peak (99 [eV] and 103.3 [eV] respectively for Al Kα) are visible, confirming a lack of Cu ablation as expected.

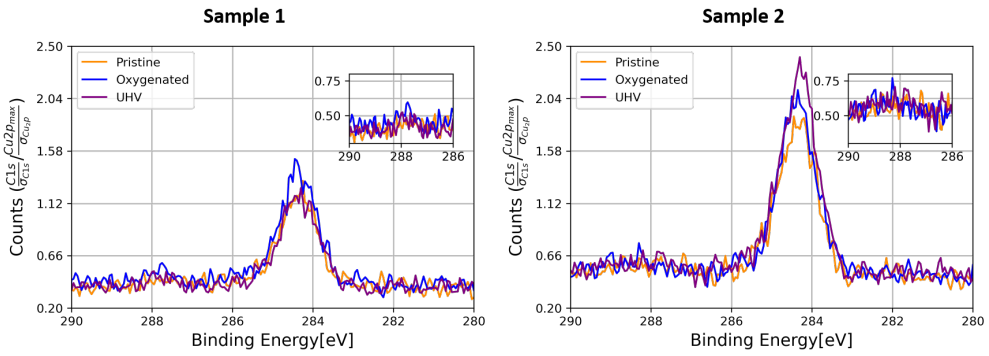

Figure 7: C1s spectra (PE = 100 [eV]) from two different samples of the single-shot, non-ambient regimes. Each plot contains one pristine measurement, one spot illuminated in UHV and the other illuminated in oxygenated conditions.

In Figure 7 a selection of C1s spectra are shown. Here two Binding Energies are of interest: a large peak at 284.5 [eV] and a much smaller one at 288 [eV]. These correspond with C(0) and C=O bond respectively [12]. This indicates a sizable (relative to Cu2p) layer of pure carbon deposited on the surface, though only a small portion seems to have bonded with native oxygen. In addition the relative carbon proportions vary between spots of different illumination conditions though they vary between different regions and samples, indicating a local adsorption variation than a systematic laser-induced change.

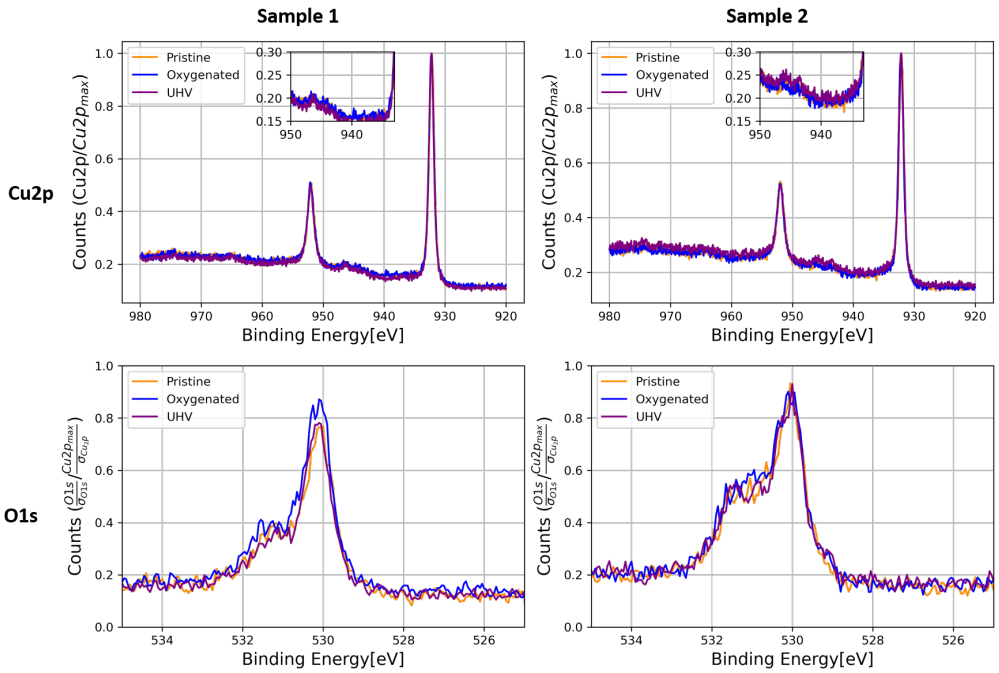

Figure 8: Cu2p and O1s spectra (PE = 100 [eV]) from two different samples under the single-shot, non-ambient regimes (upper and lower). Each plot contains one pristine measurement, one spot in UHV and the other in oxygenated condition. spectra of the same color are from the same spot.

Figure 8 shows a difference in Cu oxidated species between samples. Here Sample 1 shows a dominance of Cu_2O/Cu(0) with the 2 main peaks (932 [eV] and 952 [eV]) from 2p 3/2 and 2p 1/2 spin-orbit splits. The main peaks' positions and the weak satellites between 940 [eV] and 950 [eV] are indicative of Cu_2O. This corresponds to the 530.2 [eV] peak in O1s spectra. In contrast sample 2 shows more Cu species with a small shoulder after the two Cu2p main peaks with a more pronounced shake-up peak in the same $940 - 950$ [eV] range. The combination of the two points to the existence of CuO and $Cu(OH)_2$, with a higher BE (933.8 [eV] and 934.7 [eV] respectively for their 2p3/2 peaks) and well-defined shake-up peaks.This corresponds with an increase in the higher BE shoulder in O1s. The higher BE shoulder at 531 [eV] to 532 [eV] could be of multiple sources: defective Cu_2O and CuO, $Cu(OH)_2$ and carbon oxides all contribute in this region.

Spectra of individual elements in vacuum mostly correspond with their oxygenated

counterparts. After repeated experimentation (6 spots illuminated in UHV and another 6 in 10^{-2} mbar), all Si2p spectra exhibit no identifiable peaks within the expected binding energy ranges. C1s spectra also show no consistent differences between the two regimes, with Cu(0) consistently larger than the C=O contributions. This is also the case for samples illuminated in ambient, demonstrating a lack of detectable laser-induced changes on carbon and silicon oxidation species. A similar thing can be said for copper and oxygen for the non-ambient regimes: for four out of six spectra the former consistently have a higher peak at 530 [eV] and a higher BE shoulder around 531.25 [eV], and the latter having its main peaks at 952 [eV] and 932.2 [eV] that is indicative of a Cu(0)/Cu_2O mixture. While some spectra shows a small quantity of CuO/$Cu(OH)_2$, these are delineated by different samples rather than different illumination regimes. This is not the case for ambient experiments, where indications of Cu oxidation species change are seen.

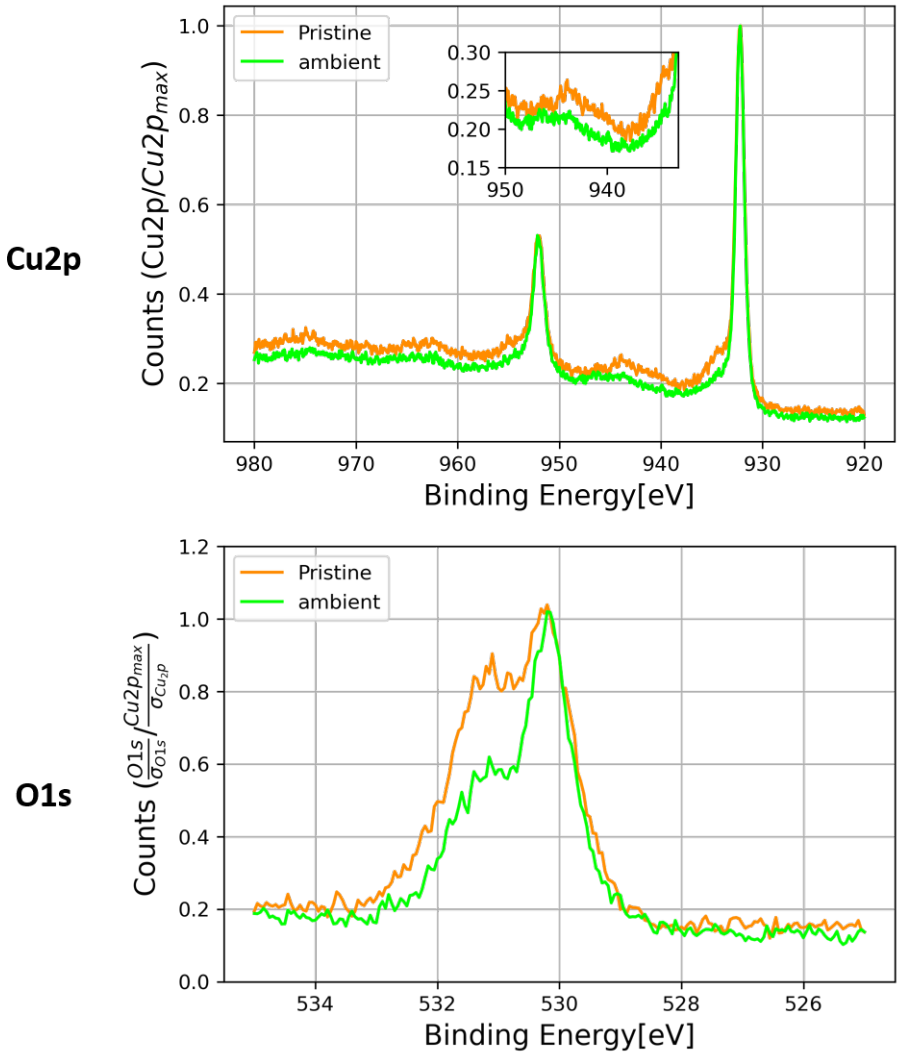

Figure 9: Cu2p and O1s spectra from samples illuminated in ambient. Here all spectra of the same color are normalized to the maximum Cu2p signal corrected with relevant cross section values sourced from Kolxpd. The inset of the Cu2p spectra shows the same spectra between 935 [eV] to 950 [eV].

Figure 9 shows an interesting variation between the pristine spot and illuminated spot(in ambient). Here we see the pristine spot showing signs of CuO/$Cu(OH)_2$ with the shake-up peaks between 940 [eV] and 950 [eV] along with the higher BE shoulders of the main Cu2p peaks at 932 [eV] and 952 [eV]. For the illuminated spot a reduction of these features are shown, which correlates with a reduction of the higher BE shoulder near 531 [eV] peak seen in O1s spectra. Note that a variety of

oxidation states are known to have peaks there, such as defective Cu_2O. and CuO, pure oxygen and hydroxyl ($Cu(OH)_2$) species [**moulder_handbook_1992**, 15].

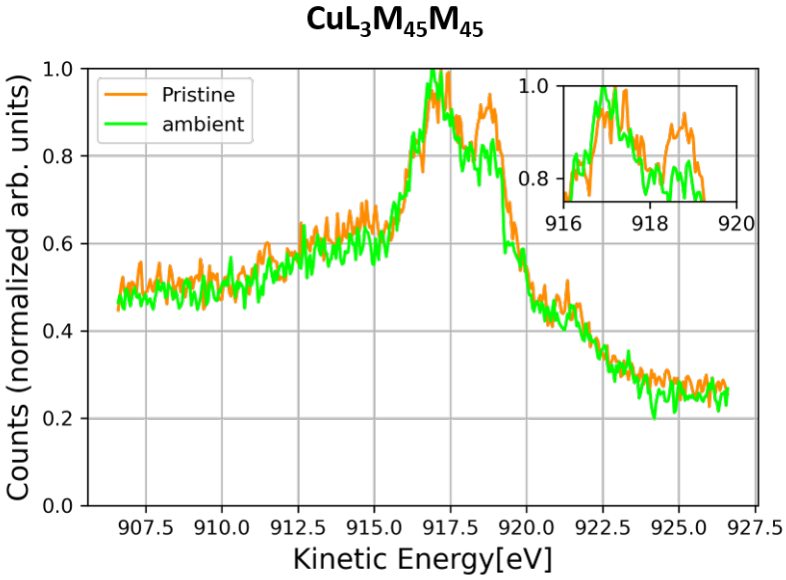

Figure 10: $CuL_3M_{45}M_{45}$ spectra from a sample illuminated in ambient for the single-shot regime. Each spectrum is normalized to its maximal signal. The inset on the upper right zooms in between Kinetic Energy (KE) = 916 [eV] and 920 [eV].

Figure 10 affirms a change in Cu oxidation species as suggested in Figure 9. Here the highest peak is around KE = 917 [eV] where the Cu_2O auger peak is expected. A reduction of another peak at KE = 918.8 [eV] is also seen when comparing the two spectra, where the Cu(0) auger peak is located. Note that the small peak between 920 and 922 [eV] is also a Cu(0) feature; this is useful as Cu oxidation states tend to have Auger spectra with multiple peaks, but only Cu(0) has a distinctive peak there. Thus it is not likely that a reduction of Cu(0) concentration occured as that small peak would vanish for the illuminated spot's Cu Auger spectrum. CuO and $Cu(OH)_2$ has its peaks at KEs' of 918 [eV] amd 916.5 [eV] respectively. These regions show little difference between the pristine and illuminated spot.

Ambient spectra for single-shot regimes shows relatively large change of copper and oxygen species from illuminated spots compared with their pristine counterparts in

Figure 8. With repeated experimentation, Cu2p and O1s spectra together show a consistent difference (four out of five spectra) between the pristine and illuminated regions of copper samples, albeit at varying levels. Reductions of the higher BE shoulders in O1s spectra from illuminated spots are correlated reductions of their counterparts in Cu2p spectra. Shake-up peaks in Cu2p spectra also show a level of reduction when comparing illuminated spots to pristine ones. This along with a reduction at KE = 918.8 [eV] in the Cu auger peak cements a detected oxidation difference seemingly laser-induced. To identify potential oxide growth quantitatively the spectra are fitted using Kolxpd to calculate if there is a change in ratios. Here the data are fitted to represent the integrated area of the spectra and not of specific species identification.

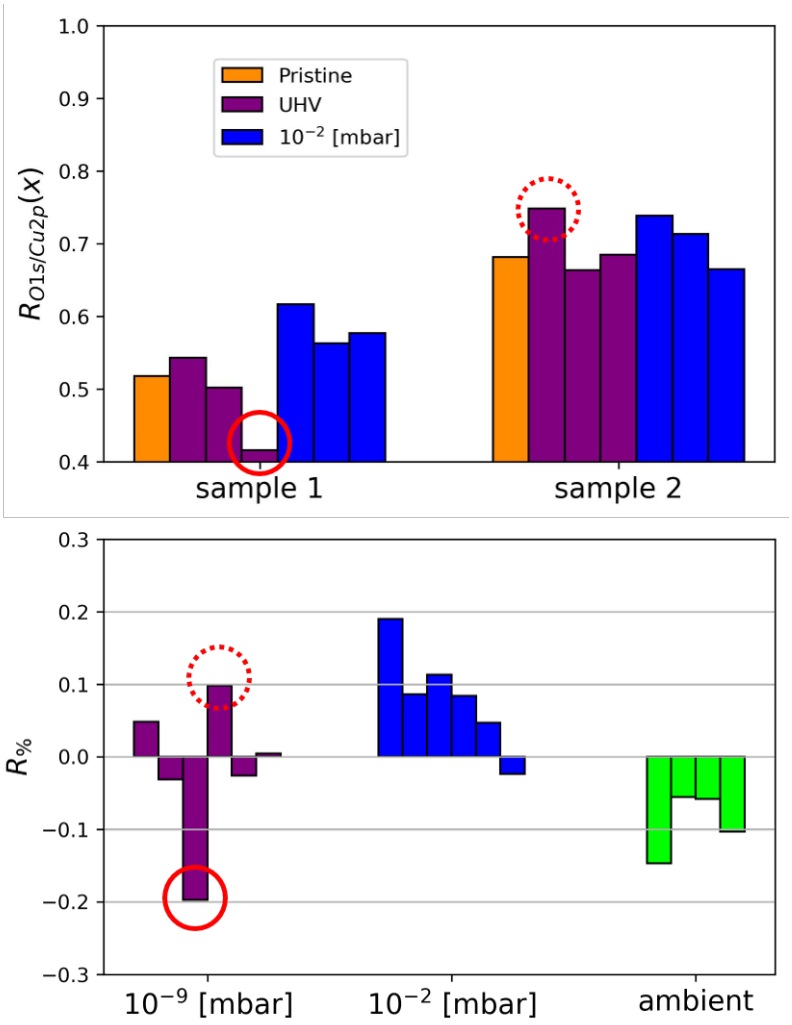

Figure 11: Relative oxidation changes across different pressure regimes ($R_{\%} = [R(illuminated) - R(pristine)]/R(pristine), R(x) = \mathrm{O1s_x/Cu2p_x}$). Values from each element were obtained by integrating over respective spectra via Kolxpd fitting, then divided by its cross section.

Figure 11 shows a consistent change in oxygen concentrations from copper surfaces illuminated in different atmospheric conditions. Here the ratio of oxygen over copper is calculated for each illuminated spot corrected with cross section values, then this is compared with its counterpart from pristine spots. The result then shows the relative growth/reduction of oxygen concentrations of illuminated samples. For the ambient and oxygenated cases consistent growth/reductions were seen. However when compared to results from UHV illumination the amount of such

changes are mostly not significant. The outliers however correspond to spots whose Cu2p spectra deviate from their pristine counterparts, atypical behavior compare to the other spectra that do in the same pressure regime. This connection of spectral shape differences and relative oxidation changes are the most apparent between different samples as seen in Figure 8.

4.3.2 Single- v.s. Multi-shots Regimes

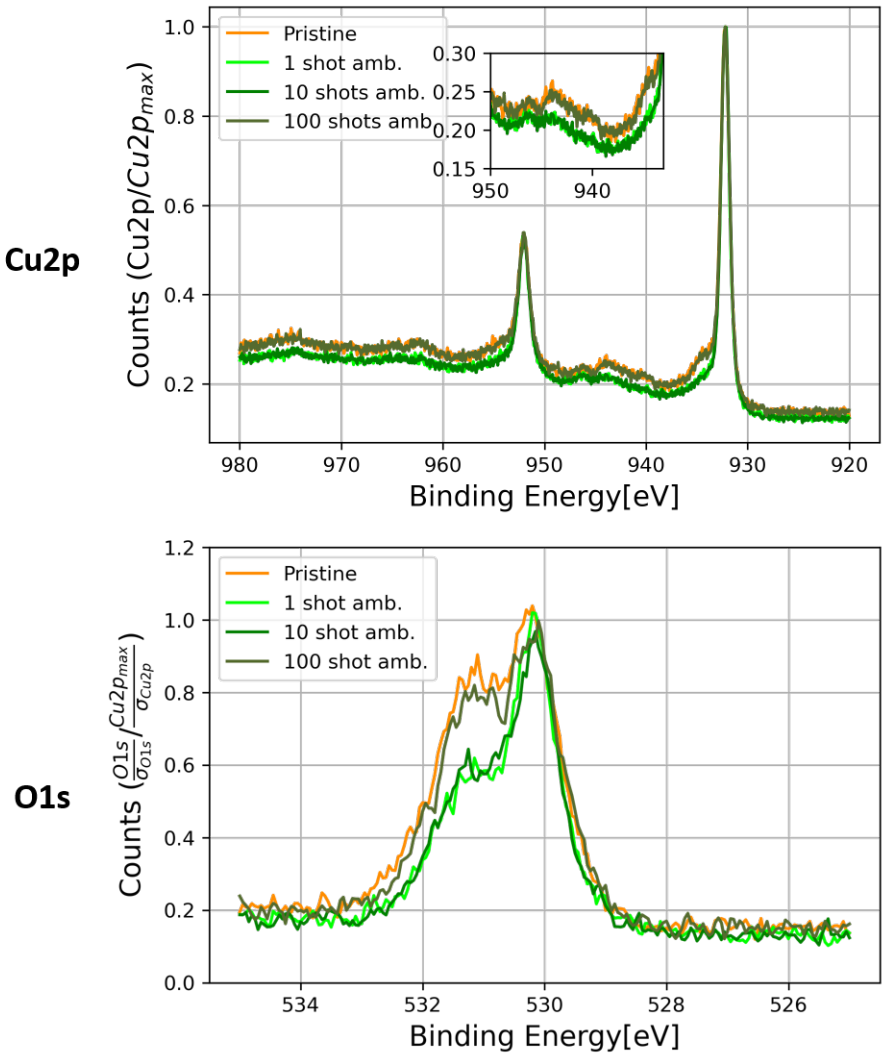

Figure 12: Cu2p and O1s spectra from samples illuminated in ambient for single- and multi-shots regimes. Here all spectra of the same color are normalized to the maximum Cu2p signal corrected with relevant cross section values sourced from Kolxpd. The inset of the Cu2p spectra shows the same spectra between 935 [eV] to 950 [eV].

Figure 12 shows an inconsistent oxidation species change between different illumination regimes. Reduction of higher-BE shoulders as seen in the single-shot case is not exhibited for the 100 shots case, with the latter exhibit the same oxidation species distribution as the pristine spot. The spot illuminated with 10 consecutive pulses

show similar spectra to the single-shot case, with little difference in peak positions nor spectral widths. This shows a lack of correlation between increasing number of pulses and oxidation changes.

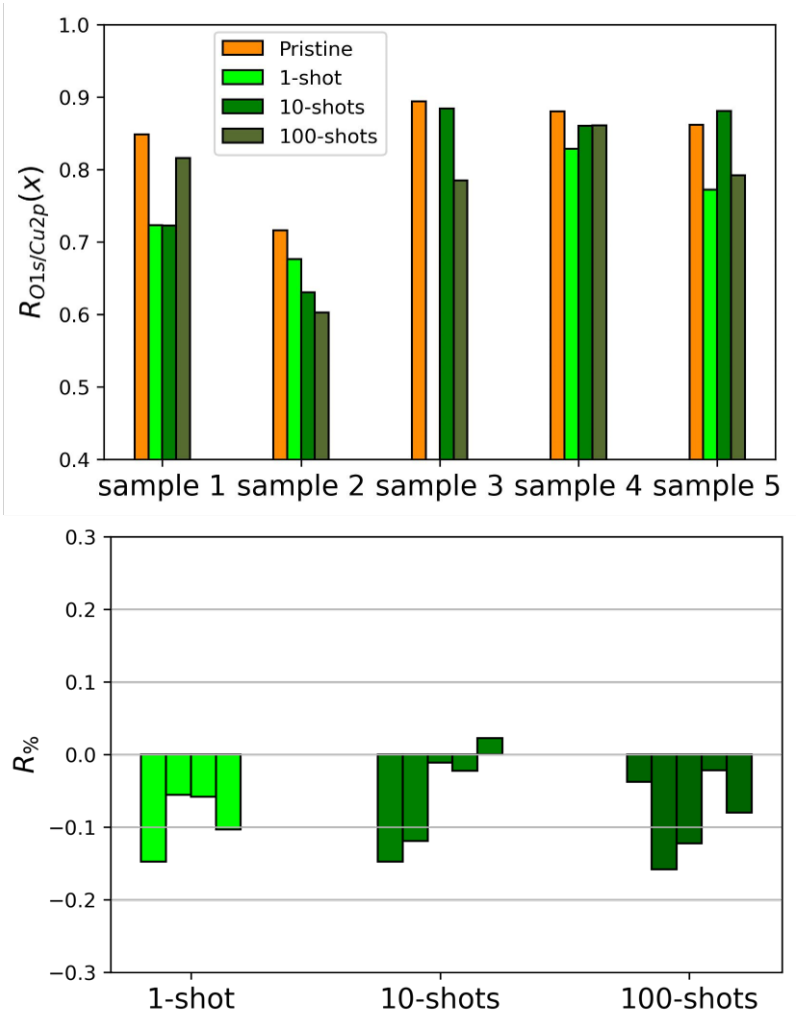

Figure 13: Relative changes of oxidation under single- and multi-shot regimes ($R_{\%} = [R(illuminated) - R(pristine)]/R(pristine), R(x) = \mathrm{O1s_x/Cu2p_x}$). Values from each element were obtained by integrating over respective spectra via Kolxpd fitting, then divided by its cross section. Data compiled in the lower plot are done sequentially from sample 1 to 5.

Figure 13 shows a lack of inter-illumination regime differences in oxygen concentration. The relative ratio increases are calculated the same way as in Figure 11. The results show a mostly consistent maximum of $\approx 15\%$ increase in oxygen

concentration for all cases. The minimum is lower for the multi-shot regimes with $\pm 2.5\%$, unlike the 5% seen in the single shot case. This indicates a lack of oxide formation/removal with increasing number of pulses. However, unlike Figure 11 a comparatively consistent reduction of oxygen concentration is observed across different illumination regimes.

Repeated experimentation for different illumination regimes (four spots with single-shot, five spots each for 10 shots and 100 shots) show a lack of inter-regime changes. Spectra from Cu2p and O1s indicate either an adherence to either the trend seen for the pristine case or the single-shot case as seen in Figure 12. Ratio calculations are also inconclusive with a wide range (15% to $\pm 2.5\%$) of oxygen concentrations for multi-shot regimes. What is note worthy is that lower $R\%$ i.e. similar oxygen concentrations between illuminated and pristine spots corresponds to a similarity of peak positions in Cu2p and O1s. In combination with Figure 13, where the deviation of $R_{\%}$ from 0% is also correlated with a deviation from pristine spectral trends, shows a relation between oxidation species change and

5 Discussion

Results show that while there seems to be little laser-induced oxidation growth, there are indications of compositional change as a product of UV illumination. There can be multiple possible interpretations of what kind of changes took place, but with the limitations of the approach taken it is far from clear if these are responsible for the different ablation thresholds of copper films in vacuum and ambient.

5.1 Chemical changes & their impacts

Carbon contamination does not play a direct role in LIO. This is seen with Figure 7 and 6, where little oxidation states have been observed for both. For carbon while the peaks do vary between samples, only the pure C(0) peak at 284.5 [eV] vary significantly; C=O peaks at 288 [eV] are always much smaller than the former and exhibits no significant deviations from the pristine spectra. The small C=O peak indicates that carbon-oxygen bonding does not significantly compete with any copper oxidation process when compared to the large changes of the O1s higher-binding energy shoulders between pristine and ambient-illuminated Cu surfaces seen in Figures 9 and 12. A similar thing can be said for silicon.

The silicon substrate have little detectable effect on Cu oxidation states. For pure Si(0) nor SiO_2 no visible peaks are detected for pristine and illuminated samples, although with more thorough measurements e.g. multiple XPS sweeps one might be able to detect traces of it due to Si2p's small cross section (0.01112 for a X-ray source of 1486.6 [eV]). What is not known is if the oxygen contribution at the Cu-Si/SiO_2 intermixing layer has an effect on Cu oxidation. Preliminary threshold testing of Si substrate with native SiO_2 layer indicates a damage threshold of > 0.6 [J/cm^2] in ambient for all illumination regimes (see Figure 15 in Appendix). This is much larger than the fluences the Cu samples are illuminated with as seen from Figure 5. Thus it is not expected for the substrate to have extensive interactions with Cu. However, the intermixing layer may have a different tolerance towards laser damage than the SiO_2 surface. In addition the oxygen concentration nor the thickness of

the SiO_2 layer are known, thus the source of oxygen cannot be fully attributed to Cu surface oxidation. Nevertheless as both bulk and thin-film copper are known to oxidize readily under oxygen exposure and the XPS measurement depth is <10nm, one can expect oxidation changes measured to be mainly surface driven.

UV Illumination of Cu samples in different pressure regimes show a significant difference of Cu oxidation states between UHV and ambient conditions. In particular we see an increase in Cu_2O after illumination. This is the most apparent with a comparison of Figures 8 (UHV) and 9 (ambient), with the latter exhibiting changes in higher-binding energy shoulders of Cu2p and O1s and a relative reduction of the Cu2p shake-up peaks between 940 and 950 [eV]. The result is a dominance of the 530.2 [eV] O1s peak and 932.2-952 eV Cu2p peaks, typical indications of Cu_2O. This corresponds with a reduction of oxygen concentration as seen in Figure 11, where the spectra corresponds to the largest reduction (15%) seen in ambient (for reference see the collected table of ratios in the Appendix). While the wide variation range of oxygen concentration change (-20% to $+10\%$) seen in the UHV regime may seen to disprove this point, they largely come from two points that deviates from the general trend as seen in the marked entries in Figure 11. Thus those two points are more likely to be outliers than defining the trend seen for UV illumination in the UHV regime. What is interesting is that if this is true, the general trend of increasing oxygen concentrations in the oxygenated regime (10^{-2} [mbar]) is then driven by a different process as it does not show the same changes the ambient regime exhibits Cu2p and O1s spectra of spots illuminated in the oxygenated regime do not change in correspondence with the detected oxygen concentration increases. This is again seen with a comparison of Figures 8 (UHV) and 9, where both spectra do not show an increase in oxidation species change in the inverse manner for ambient regime spectra. While the amount of growth varies between spots, spots with the largest growth show much smaller spectral changes than one would expect. As an example the highest amount of growth seen in Figure 11 of nearly 20% corresponds to the Oxygenated/Pristine spectra from sample 1 shown in Figure 8. Here a much smaller change of both Cu2p and O1s spectra is seen compared to the ambient

case previously. This seems to indicate that changes in oxygen concentration is not proportional to higher-binding energy shoulder changes i.e. changes in oxidation species. Nevertheless the fact that the increase in oxygen concentration did not show the same behavior exhibited by ambient regime spectra indicates that there is a link between lower oxygen concentrations and higher concentrations of Cu_2O. This is further affirmed for different illumination regimes.

Multi-shot regimes show either a relatively lower oxygen concentration accompanied by relative Cu_2O dominance or a reflection of the pristine copper surface composition. This is the most apparent in Figure 13, where O1s/Cu2p integrated signal ratios (corrected by respective cross sections) are shown in comparison with other regimes and the relative proportional changes with respective to the pristine spot. Here it is seen that only one spot exhibit a slight relative oxygen concentration increase; all others are lower with varying levels. These ratios coincide with either aforementioned reductions of higher-BE shoulders in Cu2p and O1s as with the single-shot case or an adherence to pristine spectra seen in Figure 12. As this behavior is seen across different illumination regimes in the ambient and in the single-shot vacuum case, laser-induced reduction of non-Cu_2O Cu oxidation states' concentrations is the most likely explanation. This also explains the different oxygen concentrations shown between Figures 11 and 13, as the latter contain samples with higher concentrations of non-Cu_2O species. This is most likely why for ambient regimes the general oxygen concentration is higher than UHV and oxygenated regimes. This level of certainty, though not definite by any means, cannot be conferred to the kinds of oxidation species reduced as this theory would imply.

The high-binding energy shoulders seen in O1s spectra as per Figure 9 can have multiple contributions. This is due to the fact that multiple oxidation species occupy the same peaks seen in Cu2p and O1s spectra. These include defective CuO and Cu_2O as reported by Biesinger et al., and $Cu(OH)_2$ [15]. The latter is due to adsorbed water films dissociating into OH^- and H^+ [29]. It should be noted that while pure O(0) peak is also at 531 [eV] we can expect such adsorption to contribute little as the vacuum chamber pumps are adequate in removing non-chemisorbed oxygen

within the chamber. As the higher-BE shoulders in O1s spectra have a typical width of around 1 [eV], it can be from any of these species. In addition Cu2p spectra do not show the difference between defective and lattice copper oxides, and spectra for $Cu(OH)_2$ and CuO are vary similar in both their main peaks and shake-up peaks positions. Thus multiple interpretations of this laser-induced reduction can exist.

Multiple co-existing interpretations can be applied to explain the seeming laser-induced reduction of non-cuprous oxide copper species. The first is the removal of water films via evaporation. This leads to less hydroxyl speciation as the water vapor leave the surface. The second is a selective removal of copper species of higher oxygen concentrations i.e. CuO and $Cu(OH)_2$. The first theory is fairly simple and requires little assumptions. Its flaw is that it does not agree with existing literature, with ablation experiments of bulk copper demonstrating an enhancement of $Cu(OH)_2$ after illumination [20]. It should be noted though that such studies experiment with multi-shot regimes of a much higher repetition rate on bulk copper, which is not directly applicable to this. The second theory by contrast is in agreement with literature, as CuO in particular has a lower thermal penetration depth compared to Cu_2O and as such is easier to remove [28]. This has been confirmed in the same study with a KrF excimer laser of a similat laser profile, where CuO removal was more efficient than Cu_2O removal. This however would imply that the detected reduction is a product of sample preparation and not the ambient oxygen as samples illuminated in UHV and oxygenated conditions have less non-Cu_2O concentrations. In addition only defective CuO are removed as lattice CuO is at 529.68 [eV], near the lattice Cu_2O. Thus if this is true then there must be a large concentration of defective copper oxides on the surface. This then raises the question of where such large formations of defect formations come from. In addition both of these possibilities cannot provide an answer for the oxygen concentration increase seen for the oxygenated single-shot regime.

5.2 Flaws & Potential Improvements

XPS measurement accuracy of copper samples are limited by inaccuracies in positioning the measurement spot. As the illuminated spot is only slightly bigger ($\approx$1 [mm]) than the measurement range (0.8 [mm] diameter), the-to the naked eye-invisible spots are difficult to detect accurately. As no material is expected to be removed, a simple detector of copper/Si signals is of little help. While the pockets help aiming by establishing its position using an electron analyzer to detect copper signal (and lack thereof at the borders), it is often not clear if the estimated center via said borders is where the illuminated spot lies. Defective film deposition and the lack of high precision in illumination meant that relative to the pocket's center different spots can have different positions, which leads to more pristine regions of the copper surface being detected. This is the most likely explanation of inconsistent changes of Cu2p & O1s spectra under illuminated spots as the their untreated counterparts are much more stable. This lack of knowledge of the equipment conditions as it is being used is also the case for UV illumination of samples, though this time with the laser itself. The spatial profile and fluence of the UV laser as it illuminates the copper samples are unknown due to experimental constraints. This is due to a lack of equipment compatible with the vacuum setup that can characterize the beam in situ. This meant that the fluence deposited into the copper samples are unknown. This is partially corrected by measuring the fluence before and after measurements with zero attenuation, but nevertheless for fluences not detectable by the powerometer ($< 0.6 J/cm^2$) the fluence variation is unclear. Moreover, it is unclear how uniform the fluence is when deposited onto the sample, putting into doubt if different ablation behaviors could the the result of varying spatial profiles. Nevertheless it can be determined by the slow linear decrease of ablated area at higher fluences seen in Figure that there is some level of uniformity for all the data points, though the difference of trends seen between vacuum and ambient samples could be impacted by this since the laser was realigned after vacuum illumination was done. The low number of samples also contribute to this lack of confidence for identifiable trends.

A low number of data points were generated from XPS measurements and images of

illuminated spots, limiting the precision of quantification done. Typical data points for threshold determinations in particular often ranges in the hundred and thousands, much larger than what is done here. It should be noted however that this speaks little of the trends and general differences for ablation thresholds under vacuum and ambient, as more data points merely reduces random errors. Similarly more measurements may not be helpful for XPS determinations as the problem is primarily a limitation of the approach taken. Thus while it is unclear how reliable the quantified values for the ablation threshold and compositional changes, the trends identified should keep as demonstrated. It should be kept in mind however that Laser-Induced Chemistry is not the only process known to affect damage thresholds.

The difference between vacuum and ambient ablation thresholds could have other effects independent of chemical changes induced by the laser. The ambient atmosphere is widely know to suppress plumes formed from ejected material, which would then have a strong hand in the ablation threshold [20]. In addition the existence of water films have been recorded to change damage behavior with UV illumination [30]. Suffice to say there is plenty to investigate and built upon this proof of concept experimentation.

6 Outlook

We have shown that Copper samples demonstrate a clear difference in ablation threshold when illuminated, using a UV laser, under different atmospheric conditions. This difference was quantified to show that there is a 66.7% difference in ablation threshold between samples illuminated under vacuum and their ambient counterparts. Investigations into whether Laser-Induced-Oxidation (LIO) is the result of this were done by illuminating samples near the ablation threshold and measure said spots via X-Ray Photo-electron Spectroscopy (XPS). XPS results show a inconsistent reduction of CuO & Cu(OH)2 as a product of illumination in the pre-ablation damage regime across different oxygen pressures (10^{-9} mbar, 10^{-2} mbar & 1bar). Lack of knowledge of experimental conditions and equipment limitations are identified as the greatest hurdle to overcome to make any definite conclusions on the impact of such oxide species compositional changes.

A variety of improvements and additional avenues of investigations can be opened to evaluate LIO effects in a more quantitative manner. Aside from the obvious issues of aiming the XPS and laser profile determinations, it may be useful to clean the copper surfaces via hydrogen reduction to be rid of the excess oxygen and carbon. This will open up the availability of copper for oxidation and thus a more pronounced effect of LIO, for sub-ambient pressure regimes, should be seen. Should a more streamlined process be established XPS measurements of spots before and after illumination will also increase the accuracy of detecting potential chemical changes. This in conjunction with a illuminated sample that has the spot much larger than the XPS measurement range can help both the accuracy and precision of XPS analyses. More time into fitting the XPS data to have a deeper understanding of existing oxidation species will help realize what species exist on the samples prior and after illumination. This in conjunction with other surface characterization techniques of higher sensitivity such as the Atomic Force Microscopy can give one a much better understanding on what is happening at the surface.

References

[1] D. R. Paschotta, *Time-resolved spectroscopy*, https://www.rp-photonics.com/time_resolved_spectroscopy.html (visited on 09/05/2023).

[2] J. P. Dougherty and S. K. Kurtz, Journal of Applied Crystallography **9**, 145 (1976).

[3] M. Soileau, in *Laser-induced damage in optical materials*, edited by D. Ristau, 1st ed. (CRC Press, Boca Raton, 2015), pp. 3–8.

[4] D. Ristau, in *Laser-induced damage in optical materials*, 1st ed. (CRC Press, Boca Raton, 2015).

[5] J. Brannon, IEEE Circuits and Devices Magazine **6**, 18 (1990).

[6] S. V. Starinskiy, Y. G. Shukhov, and A. V. Bulgakov, Applied Surface Science **396**, 1765 (2017).

[7] C. R. Giuliano, Applied Physics Letters **5**, 137 (2004).

[8] J.-Y. Natoli, L. Gallais, H. Akhouayri, and C. Amra, Applied Optics **41**, 3156 (2002).

[9] L. Jensen, M. Jupé, H. Mädebach, H. Ehlers, K. Starke, D. Ristau, W. Riede, P. Allenspacher, and H. Schroeder, in Laser-induced damage in optical materials: 2006, Vol. 6403 (Jan. 15, 2007), pp. 291–300.

[10] D. Basting and U. Stamm, **215**, 1575 (2001).

[11] R. Rottenfusser, E. E. Wilson, and M. W. Davidson, *Microscopy basics: reflected light microscopy*, ZEISS Microscopy Online Campus, https://zeiss-campus.magnet.fsu.edu/articles/basics/reflected.html (visited on 08/09/2024).

[12] F. A. Stevie and C. L. Donley, Journal of Vacuum Science & Technology A **38**, 063204 (2020).

[13] K. Oura, in *Surface science: an introduction*, 1st ed., Advanced Texts in Physics (Springer Berlin, Berlin, May 13, 2003), pp. 77–108.

[14] K. Siegbahn and K. Edvarson, Nuclear Physics **1**, 137 (1956).

[15] M. C. Biesinger, Surface and Interface Analysis **49**, 1325 (2017).

[16] A. García-Arellano, W. Cruz-Santos, G. García-Arellano, and J. Rueda-Paz, Optical Engineering **56**, 064102 (2017).

[17] J. S. Oh and S.-W. Kim, Optics Letters **30**, 2650 (2005).

[18] F. Wang, Z. Yue, J. Liu, H. Qi, W. Sun, M. Chen, Y. Wang, and H. Yue, Journal of Applied Physics **131**, 053101 (2022).

[19] M.-A. Beeck and W. Hentschel, Optics and Lasers in Engineering **34**, 101 (2000).

[20] D. W. Zeng, K. C. Yung, and C. S. Xie, Applied Surface Science **217**, 170 (2003).

[21] J. Jin, D. G. Shang, X. D. Liu, L. H. Zhang, Y. B. Guo, and T. Chen, Advanced Materials Research **760-762**, 413 (2013).

[22] S. Nammi, N. J. Vasa, B. Gurusamy, and A. C. Mathur, Journal of Physics D: Applied Physics **50**, 355204 (2017).

[23] T. T. D. Huynh and N. Semmar, Applied Physics A **116**, 1429 (2014).

[24] L. Torrisi, S. Gammino, L. Andò, V. Nassisi, D. Doria, and A. Pedone, Applied Surface Science **210**, 262 (2003).

[25] S. Kirkwood, A. van Popta, Y. Tsui, and R. Fedosejevs, Applied Physics A **81**, 729 (2005).

[26] L. Torrisi, A. Borrielli, and D. Margarone, Nuclear Instruments and Methods in Physics Research Section B: Beam Interactions with Materials and Atoms **255**, 373 (2007).

[27] R. W. Dreyfus, Journal of Applied Physics **69**, 1721 (1991).

[28] C. Seo, D. Ahn, and D. Kim, Applied Surface Science **349**, 361 (2015).

[29] S. Yamamoto, H. Bluhm, K. Andersson, G. Ketteler, H. Ogasawara, M. Salmeron, and A. Nilsson, Journal of Physics: Condensed Matter **20**, 184025 (2008).

[30] S. Lai, Y. Liu, L. Gong, Y. Zhao, C. Zhang, and B. Han, Optics & Laser Technology **168**, 109871 (2024).

7 Appendices

7.1 Attenuator calibration curve

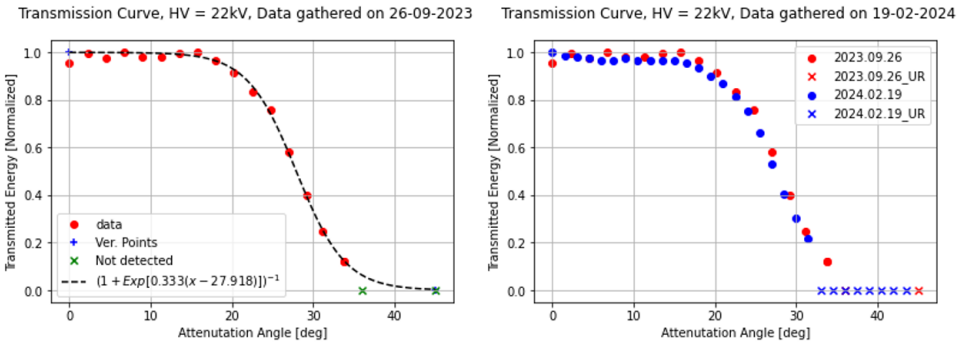

Figure 14: Detected fluences v.s. attenuation angle of the attenuator done on 2023 and 2024. The fitted attenuation curve used to calculate fluence is exhibited on the left.

Figure 14 shows the stability of the attenuator over time. Here the reduction of intensity is tested by measuring said quantities of specific attenuation angles. Here we see that after a few months the results are very similar, hence the attenuator did not degrade over time. In addition the calibration curve used to calculate the deposited pulse energy, as the powermeter cannot measure fluences lower than 0.6 $[\mathrm{J/cm^2}]$, as shown in the left plot is shown to be accurate as the data it is based off of corresponds to repeated test a few month later as shown.

7.2 Silicon damage by UV illumination

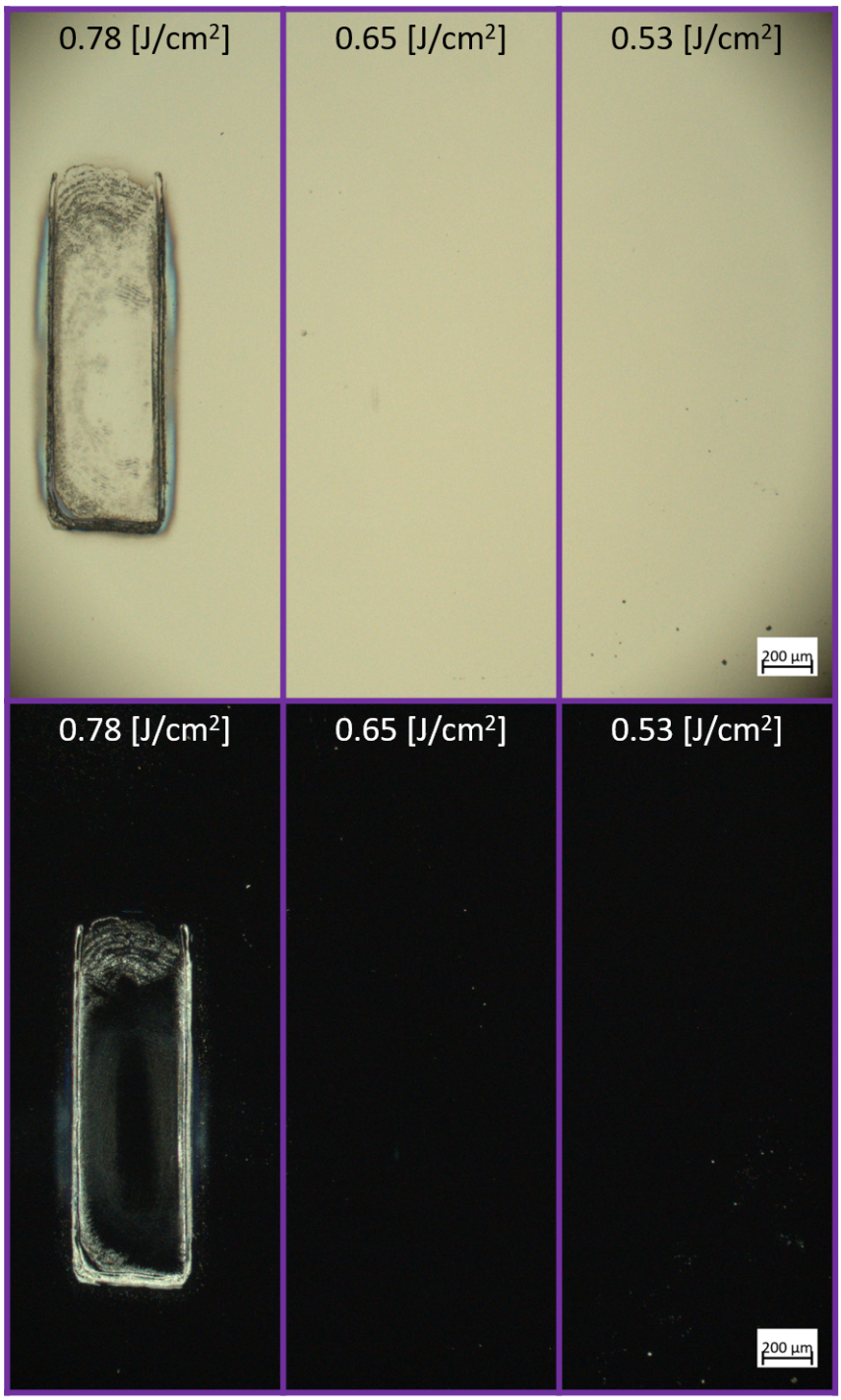

Figure 15: Bright-field and dark-field images of Si substrate surface after 100 consecutive UV pulses. Substrate known to have a native oxide layer on top. Fluences of a single pulse of the repeated illumination are written on top of each image.

Figure 15 shows a preliminary analysis of Si damage threshold. Here the same substrates used for copper thin-film deposition is used. The substrate has a layer of native silicon oxide with unknown thickness. The images here show that the damage threshold as defined in the Results section is between 0.78 $[J/cm^2]$ and 0.65 $[J/cm^2]$, much larger than any of the damage thresholds for thin-film copper.

7.3 Ratios between chemical elements of interest

Vacuum/Oxygenated Sample 1	Cu2p/O1s	Cu2p/C1s	O1s/C1s	Cu2p/pristine	O1s/pristine	C1s/pristine
oxygenated spot 1	1,62	1,22	0,75	0,87	1,03	1,10
oxygenated spot 2	1,78	1,33	0,75	0,92	1,00	1,07
oxygenated spot 3	1,73	1,18	0,68	0,90	1,00	1,18
pristine	1,93	1,55	0,80	1,00	1,00	1,00
vacuum spot 1	1,84	1,25	0,68	0,96	1,01	1,19
vacuum spot 2	1,99	1,62	0,81	1,06	1,03	1,01
vacuum spot 3	2,41	2,09	0,87	1,25	1,01	0,93

Vacuum/Oxygenated Sample 2	Cu2p/O1s	Cu2p/C1s	O1s/C1s	Cu2p/pristine	O1s/pristine	C1s/pristine
oxygenated spot 1	1,35	0,58	0,43	0,81	0,88	1,16
oxygenated spot 2	1,40	0,75	0,53	0,94	0,98	1,03
oxygenated spot 3	1,50	0,77	0,51	0,96	0,93	1,03
pristine	1,47	0,82	0,56	1,00	1,00	1,00
vacuum spot 1	1,34	0,53	0,40	0,78	0,86	1,22
vacuum spot 2	1,51	0,72	0,48	0,91	0,89	1,04
vacuum spot 3	1,46	0,76	0,52	0,95	0,96	1,02

Ambient Sample 1	Cu2p/O1s	Cu2p/C1s	O1s/C1s	Cu2p/pristine	O1s/pristine	C1s/pristine
1-shot	1,38	1,55	1,12	1,07	0,91	1,28
10-shots	1,38	1,74	1,26	1,07	0,91	1,14
100-shots	1,23	1,67	1,36	1,00	0,96	1,11
pristine	1,18	1,85	1,57	1,00	1,00	1,00

Ambient Sample 2	Cu2p/O1s	Cu2p/C1s	O1s/C1s	Cu2p/pristine	O1s/pristine	C1s/pristine
1-shots	1,48	0,97	0,65	1,00	0,96	1,11
10-shot	1,59	1,21	0,76	1,07	0,91	1,28
100-shots	1,66	1,15	0,69	1,07	0,91	1,14
pristine	1,40	1,18	0,85	1,00	1,00	1,00

Ambient Sample 3	Cu2p/O1s	Cu2p/C1s	O1s/C1s	Cu2p/pristine	O1s/pristine	C1s/pristine
1-shots	1,14	0,95	0,83	0,99	0,97	0,98
10-shots	1,13	0,94	0,83	0,98	0,96	0,97
100-shot	1,27	0,85	0,66	1,03	0,90	1,14
pristine	1,12	0,93	0,83	1,00	1,00	1,00

Ambient Sample 4	Cu2p/O1s	Cu2p/C1s	O1s/C1s	Cu2p/pristine	O1s/pristine	C1s/pristine
1-shot	1,21	0,85	0,71	1,11	1,04	0,90
10-shots	1,16	0,75	0,65	1,08	1,06	1,00
100-shots	1,16	0,72	0,62	1,05	1,03	1,00
pristine	1,14	0,69	0,61	1,00	1,00	1,00

Ambient Sample 5	Cu2p/O1s	Cu2p/C1s	O1s/C1s	Cu2p/pristine	O1s/pristine	C1s/pristine
1-shots	1,30	0,78	0,61	0,99	0,89	1,06
10-shot	1,26	0,84	0,66	0,98	0,90	0,98
100-shots	1,14	0,62	0,54	0,87	0,89	1,19
pristine	1,16	0,84	0,73	1,00	1,00	1,00

Figure 16: Calculated ratios of highlighted elements from various samples. Ratios were calculated from comparing XPS spectra intensities as stated for Figure 11.

Figure 16 shows the tabulated values of XPS signal ratios between different orbitals from elements of interest. Here the ratios are calculated by integrating over fitted XPS peaks, divide the intensities over the respective orbitals' cross sections then compare with one another. Here samples numbers correspond to samples number as seen in Figures shown in the Results section.